

Article

ANN-Based Method for Urban Canopy Temperature Prediction and Building Energy Simulation with Urban Heat Island Effect in Consideration

Fitsum Tariku * and Afshin Gharib Mombeni

BCIT Building Science Centre of Excellence, Burnaby, BC V5G 3H2, Canada; agharibmombeni@my.bcit.ca

* Correspondence: fitsum_tariku@bcit.ca

Abstract: The process of urbanization resulting from population growth is causing a transformation of natural landscapes into built environments, and contributing to a significant rise in air and surface temperatures in urban areas, resulting in what is known as the urban heat island (UHI). Ignoring the UHI effect and use of weather data from open fields and airport locations for energy and thermal comfort analysis can lead to over- and underestimation of heating and cooling loads, improper sizing of equipment, inefficiencies in the mechanical systems operation, and occupants' thermal discomfort. There is a need for computationally efficient urban canopy temperature prediction models that account for the urban morphology and characteristics of the study area. This paper presents the development and application of an artificial neural network (ANN)-based method for generating hourly urban canopy temperature and local wind speed for energy simulation. It was used to predict the urban canopy temperature of a neighborhood in downtown Vancouver and the resulting building energy consumption and indoor temperature in a typical building in the area. The results showed that the UHI effect increased the total cooling energy demand by 23% and decreased the total heating energy consumption by 29%, resulting in an overall negative effect on the total energy demand of the building, which was 18% higher in the urban area. The UHI effect also increased the number of hours of indoor temperature above the cooling set point by 7.6%. The methodology can be applied to determine the urban canopy temperature of neighborhoods in different climate zones and determine the varying urban heat island effects associated with the locations.

Keywords: building energy modeling; building energy simulation; urban heat island; urban canopy temperature



Citation: Tariku, F.; Gharib Mombeni, A. ANN-Based Method for Urban Canopy Temperature Prediction and Building Energy Simulation with Urban Heat Island Effect in Consideration. *Energies* **2023**, *16*, 5335. <https://doi.org/10.3390/en16145335>

Academic Editors: Bojan Milovanovic, Marjana Šijanec Zavrl and Marina Bagarić

Received: 15 May 2023
Revised: 22 June 2023
Accepted: 4 July 2023
Published: 12 July 2023



Copyright: © 2023 by the authors. Licensee MDPI, Basel, Switzerland. This article is an open access article distributed under the terms and conditions of the Creative Commons Attribution (CC BY) license (<https://creativecommons.org/licenses/by/4.0/>).

1. Introduction

Population growth is leading to the rapid urbanization of towns and the densification of cities, resulting in the transformation of natural landscapes into built environments. Unfortunately, this process also means that vegetation-covered and water-permeable landscapes are being replaced with heat absorbing and impermeable surfaces. The thermal characteristics of the materials [1], the absence of evapotranspiration [2], and the anthropogenic heat release to air [3,4] contribute to a significant rise in air and surface temperatures in urban areas, resulting in a phenomenon known as the urban heat island (UHI). The effects of the urban heat island are local and have a direct impact on the citizens, dwellers, and pedestrians who live and work in these areas [5]. According to Akbari et al. [6], a city with a population of over one million can have an annual air temperature that is 1 °C to 3 °C warmer than its surrounding areas. During summer nights, the temperature difference can be as much as 12 °C. This higher urban canopy temperature has a variety of impacts on urban areas, including pedestrian thermal comfort and building energy consumption.

Researchers have shown a direct relationship between the demand for air conditioning and the urban canopy temperature increase caused by the UHI effect. Akbari et al. [6] reported an increase of 5% to 10% in the peak electric demand for air conditioning in urban

areas. Similarly, Li H. [5] reported that the demand for building air conditioning increased by 1.5% to 2% for every air temperature increase of 0.6 °C in the temperature range of 20 °C to 25 °C. Li et al. [7] stated that the UHI effect could increase the average consumption of cooling energy by 19% and decrease the average heating energy by 18.7%. Despite the need to consider the different urban microclimate conditions when calculating urban buildings' energy consumption, current building energy simulation (BES) tools calculate the annual demand for cooling and heating of buildings in urban areas using a weather data file that is typically recorded at weather stations located in rural areas (parks and airports) [8]. This approach can lead to a significant error in the design and operation of buildings in urban areas. This is particularly important in big cities where 20% to 40% of the total energy consumption is attributed to the building sector [9].

Researchers use different methods to establish the urban weather file, and more importantly, the urban air temperature and wind speed, for building energy simulations and pedestrian thermal comfort analysis. One of the methods is an in situ urban weather measurement [8–11]. Although this method is straightforward for capturing the urban microclimate, it requires the deployment and maintenance of a large number of weather stations in different urban spaces with acceptable measurement uncertainty. Emamifar et al. [12] and Ho et al. [13] used statistical regression methods to predict urban air temperature from land surface temperature satellite images and field observations. The researchers used an M5 decision tree, least squares regression, support vector machine, and random forest regression algorithm to predict the daily and monthly average urban air temperatures and map the maximum summer temperatures in a city. However, accurate measurement of land surface temperature remotely can be challenging, as satellite images can be influenced by the uncertainty in the atmospheric conditions and the surface emissivity. The Town Energy Balance (TEB) model [14] and the Square Prisms Urban Canopy (SPUC) model [15] predict urban air temperature using principles of conservation of energy. In these methods, the heat and moisture fluxes from buildings, roads, and roof surfaces released into the urban canopy are linked using a network of thermal resistances [14,16,17] or both thermal resistances and capacitances [18–20] in consideration of urban heat storage. For whole-year energy simulations, Bueno et al. [21–23] developed an urban weather generator (UWG) by combining the hourly urban temperature generated using their resistance–capacitance network model with data from a metrological weather station at an airport or open field outside the city. In these energy balance-based models, buildings are represented as 2D entities or rows of square prism blocks of the same height, and their heterogeneous characteristics—including shape, height, construction type, wind-blockage effect, and variability in land surface coverage—are not explicitly accounted for.

Computational fluid dynamics (CFD)-based microclimate modeling can account for heterogeneous building characteristics and yields high-resolution urban canopy temperature and wind speed profiles. Allegrini et al. [24,25] investigated the influence of different urban morphologies on urban microclimates using CFD. They found that the morphology with cubical buildings and uniform heights had higher surface temperatures compared to buildings with complex geometry due to shadow effects, and morphologies with a lower wind flow obstruction had 2.5 °C lower temperatures compared to other morphologies. Researchers used different CFD simulation software for microclimate modeling, including the most commonly used ENVI-met [26,27] ANSYS Fluent [28,29], Phoenics [30,31], and OpenFoam [32,33]. Although the CFD tools have the capability of providing high-resolution microclimate information, their applicability is limited to short simulation periods and case studies involving the evaluation of the UHI effect mitigation measures and identifying UHI hot spots in urban areas. Due to the high computational time and resources required, these models are not currently being used to generate hourly urban temperatures and wind speeds for whole-year building energy simulations. Table 1 provides a summary of the urban weather data, energy simulation tools, simulation periods, and UHI effects on building energy consumption, as reported by various researchers.

Table 1. Summary of the literature on urban weather file and UHI effect on building energy consumption.

Researcher Location	Urban Weather Data Determination Method	Building Energy Simulation Software	Duration	Findings and Variables
Chan (2011) [34] Hong Kong	Field Measurements	EnergyPlus	6 months	10% cooling energy increase with UHII of 1.4 °C
Salvati et al. (2017) [35,36] Barcelona	Field Measurements	EnergyPlus	3 days	18–28% cooling energy increase with UHII of 2.8 °C in winter and 1.7 °C in summer
Liu et al. (2017) [11] Singapore	Field Measurements	EnergyPlus	Whole year	7% average cooling energy increase with UHII of 1–2 °C
Ma and Yu (2020) [9] Hong Kong	Field Measurements	EnergyPlus	Whole year	8% and 3% summer and winter energy consumption increase by every 1 °C
Magli et al. (2015) [8] Italy	Field Measurement	TRNSYS	Whole year	8% cooling energy increase, 20% heating energy decrease, and 7% CO ₂ emission increase by UHII of 1.4 °C
Guattari et al. (2018) [10] Italy	Field Measurement	TRNSYS	Whole year	30% cooling energy increase and 11% heating energy decrease by UHII of 1.4 °C at night and 0.84 °C during the daytime
Palme et al. (2017) [37] South America	Urban Weather Generator	TRNSYS	Whole year	15% to 200% cooling energy increase by different UHII
Litardo et al. (2020) [38] Ecuador	Urban Weather Generator	TRNSYS	Whole year	30% to 70% cooling energy increase for residential by UHII of 0.6 °C in September and 1.25 °C in February
Castaldo et al. (2018) [27] Italy	ENVI-met and Meteonorm	EnergyPlus	July 19 and January 3	10% HVAC energy reduction by 1.5 °C reduction in air temperature in summer
Aboelata and Sodoudi (2019) [26] Egypt	ENVI-met	DesignBuilder	24 h	4% (1.252 Euros/day) cooling energy decrease by 1 °C reduction in air temperature by adding 50% trees
Toparlar et al. (2018) [29] Belgium	ANSYS Fluent	EnergyPlus	1 month (July)	90% cooling energy increase in July by UHII of 3.3 °C
Fatima and Chaudhry (2017) [28] Dubai	ANSYS Fluent	Newton's law of cooling	1 h	19% cooling energy increase for every 1.22 °C temperature rise

As such, for urban areas where in situ measurements are not available or expensive to install and operate, there is a need for prediction models that are computationally efficient and that account for the urban morphology and characteristics of the study area. This paper presents an artificial neural network (ANN)-based method for generating the urban canopy temperature and local wind speed for energy and hygrothermal simulation. The method makes it possible to generate hourly urban weather data that accounts for the surrounding landscape, morphological factors, and urban heat island effects, and therefore enable a more accurate performance assessment of buildings in urban settings. The paper depicts the methods employed in the development of the ANN models, as well as their application for calculating the annual heating and cooling energy consumption of a building in a typical urban neighborhood in Vancouver, Canada.

2. Approach

In this work, an artificial neural network (ANN)-based statistical method was used to relate measurements at designated metrological weather stations such as an airport or open field to urban climate conditions. Two ANN models were developed, one for predicting urban air temperature and the other for local wind speed. The data from a metrological weather station and the ENVI-met simulation outputs form the input and the output datasets required to train and create the ANN models. A neighborhood in the city of Vancouver was identified as the study area for the development and implementation of the approach. Given that a microclimate simulation of the neighborhood using CFD for a whole year (8760 h) was not practical, six days from each month that represented the weather variability of the month were selected and simulated. The days were selected to represent the extreme and average conditions. Based on analysis of the daily maximum, minimum and median air temperature and global solar radiation, a total of 72 representative days were identified using data from a weather station near the study area. The ANN models will predict the local temperature and wind speed in the study area considering the effects of the local urban landscape, morphology, building shape, size, aspect ratio, and the albedo and emissivity of buildings and landscape surfaces. The hourly local temperatures and wind speeds generated by the ANN models were combined with other weather data obtained from a metrological weather station to create an urban weather file. Finally, the urban weather file, which incorporated the effect of UHI, was used for the building energy simulation of an office building in the study area.

2.1. Study Area

Urban neighborhoods are generally characterized with dense buildings and low vegetation cover. Accordingly, an urban area with these features and high urban surface temperature readings was chosen for this work. Figure 1a shows the urban heat islands in a section of Vancouver; the purple and red areas have higher temperatures compared to their surroundings. Based on the temperature distribution and taking the surrounding landscape into consideration, a study area in the Mount Pleasant neighborhood, shown in Figure 1b, was selected for the study. The study area is 172 m × 214 m and bounded by Manitoba Street and Columbia Street in the east and west and by West 5th Avenue and West 7th Avenue in the north and south, respectively.

The buildings in this area are concrete buildings with similar heights, 4 m to 5 m. The tallest building is 17 m tall, and the width of the street is around 20 m. The vegetation cover is negligible in the area and the color of the pavement is mostly dark.

2.2. Representative Days

As mentioned earlier, part of the datasets required for training and testing the ANN models was generated from the microclimate model simulation results and given that an hourly simulation of a full year is not practical due to extensive simulation time and calculation costs, some days in each month were selected to be representative of that month. This selection was based on different weather parameters, including air temperature, solar

radiation, and wind speed. Since the effect of cloud cover is already considered in solar radiation, this parameter is not included. As a result, the selected days represented the hottest and the coldest days, the days with the highest and the lowest solar radiation, and the days with median daily average temperature and daily total solar radiation for each month. These days were selected by ordering the days by daily average temperature and daily total solar radiation and identifying the days with the extreme and average temperatures and solar radiation. Inclusion of extreme values is essential in the training and application of the ANN models in the wide range. The same selection procedure was implemented for each month, and a weather dataset with a total of 72 days was established for the study. Figures 2 and 3 illustrate the maximum, median, and minimum of daily air temperature and daily total global solar radiation, respectively, for the study area in the year 2020.

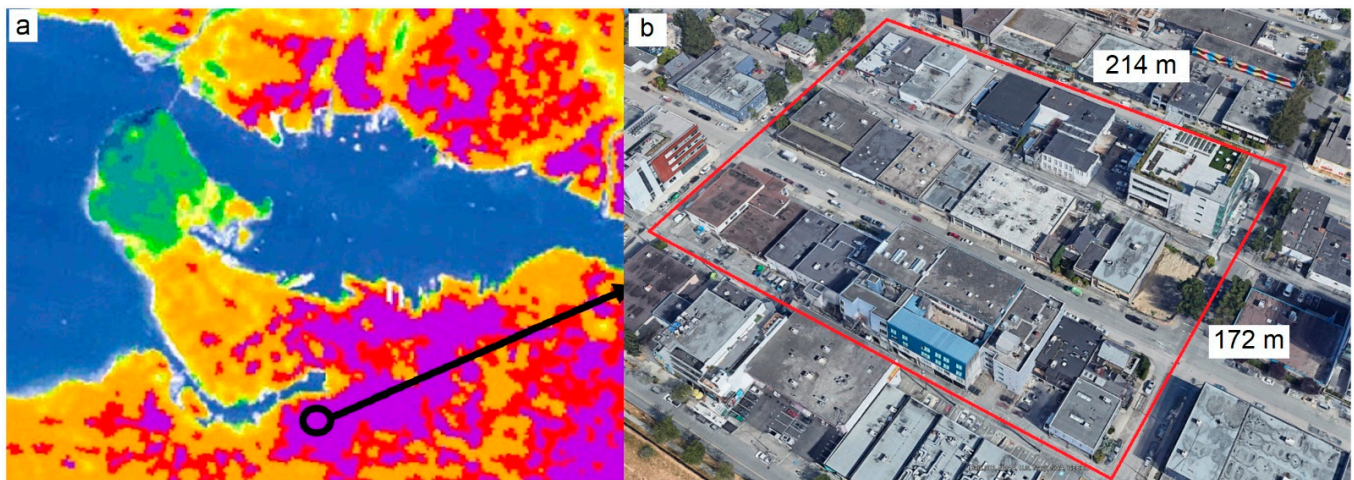


Figure 1. Vancouver thermal image (a) source: Perez (2007), and study area plan view (b).

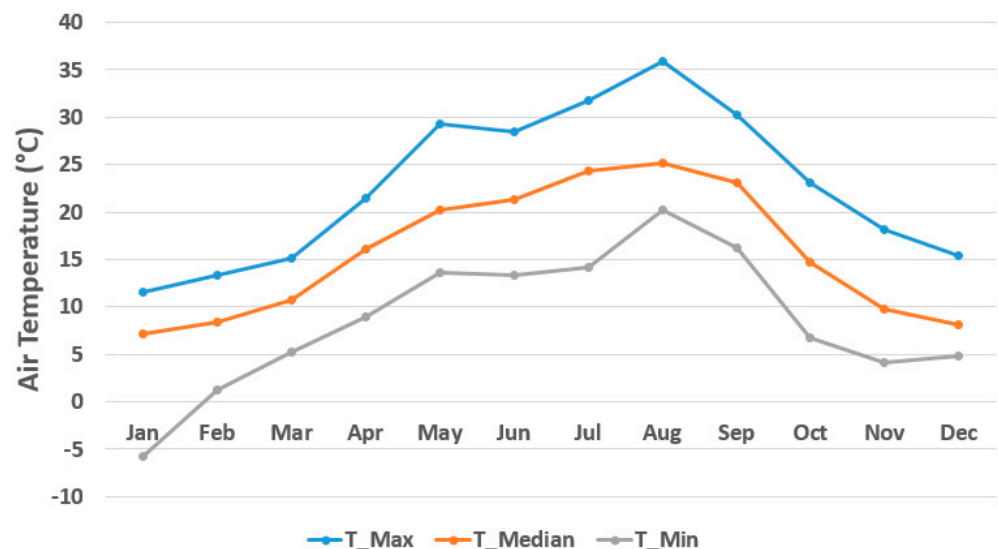


Figure 2. Maximum, median, and minimum air temperature in different months.

The six days that were selected from each month are presented in Table 2. The numbers in the table represent the day of the month; for example, the weather in January is represented by the combination of the January 3, 22, 14, 28, 25, and 10 data.

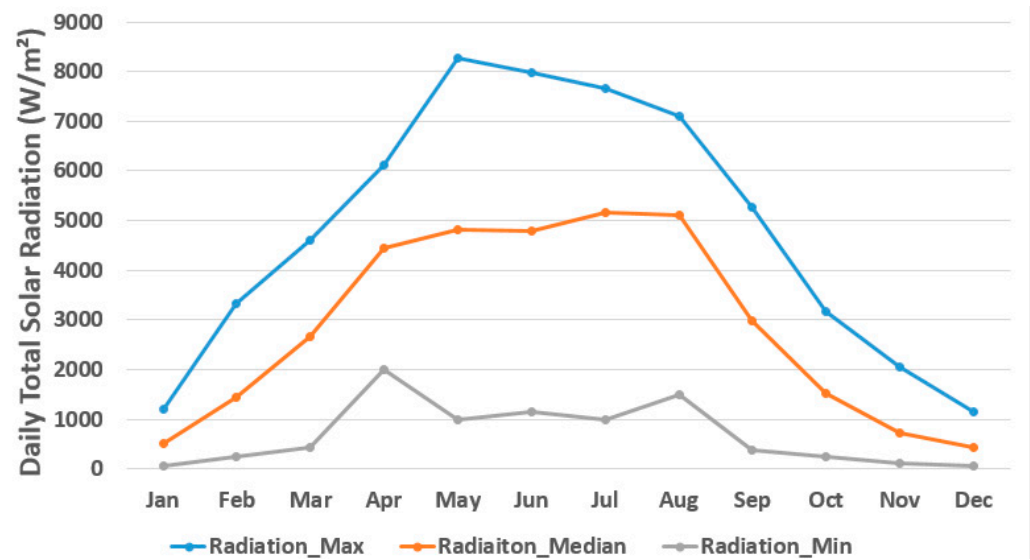


Figure 3. Maximum, median, and minimum daily total solar radiation in different months.

Table 2. Selected days in each month.

Months	T_Max	T_Ave	T_Min	Rad_Max	Rad_Ave	Rad_Min
January	3	22	14	28	25	10
February	20	12	4	24	16	7
March	21	12	2	15	8	5
April	16	12	3	18	23	22
May	28	12	2	27	1	30
June	23	11	15	7	27	9
July	21	17	1	18	13	11
August	16	10	7	4	25	21
September	10	22	26	3	2	23
October	2	16	23	3	17	9
November	2	6	9	1	13	24
December	5	12	29	2	10	21

Figure 4 illustrates the hourly air temperature and global radiation of the monthly representative days assembled for the whole year. Figure 4a–c shows the hourly air temperature and solar radiation of the days selected from each month based on maximum, median, and minimum daily average air temperature, whereas the data shown in Figure 4d–f are for days with the highest, median, and lowest daily total solar radiation. The lowest and highest hourly temperatures in the assembled dataset are -8.05 °C in January and 35.55 °C in August. The highest solar radiation is 938 W/m² in June and the winter months in general have lower solar radiation. Having a dataset with a mix of extreme and average weather conditions is essential to develop a robust ANN model.

For model warm-up and better initialization, the ENVI-met simulations were conducted for 48 h instead of 24 h; as a result, the meteorological data of the previous days were extracted and used in the simulation.

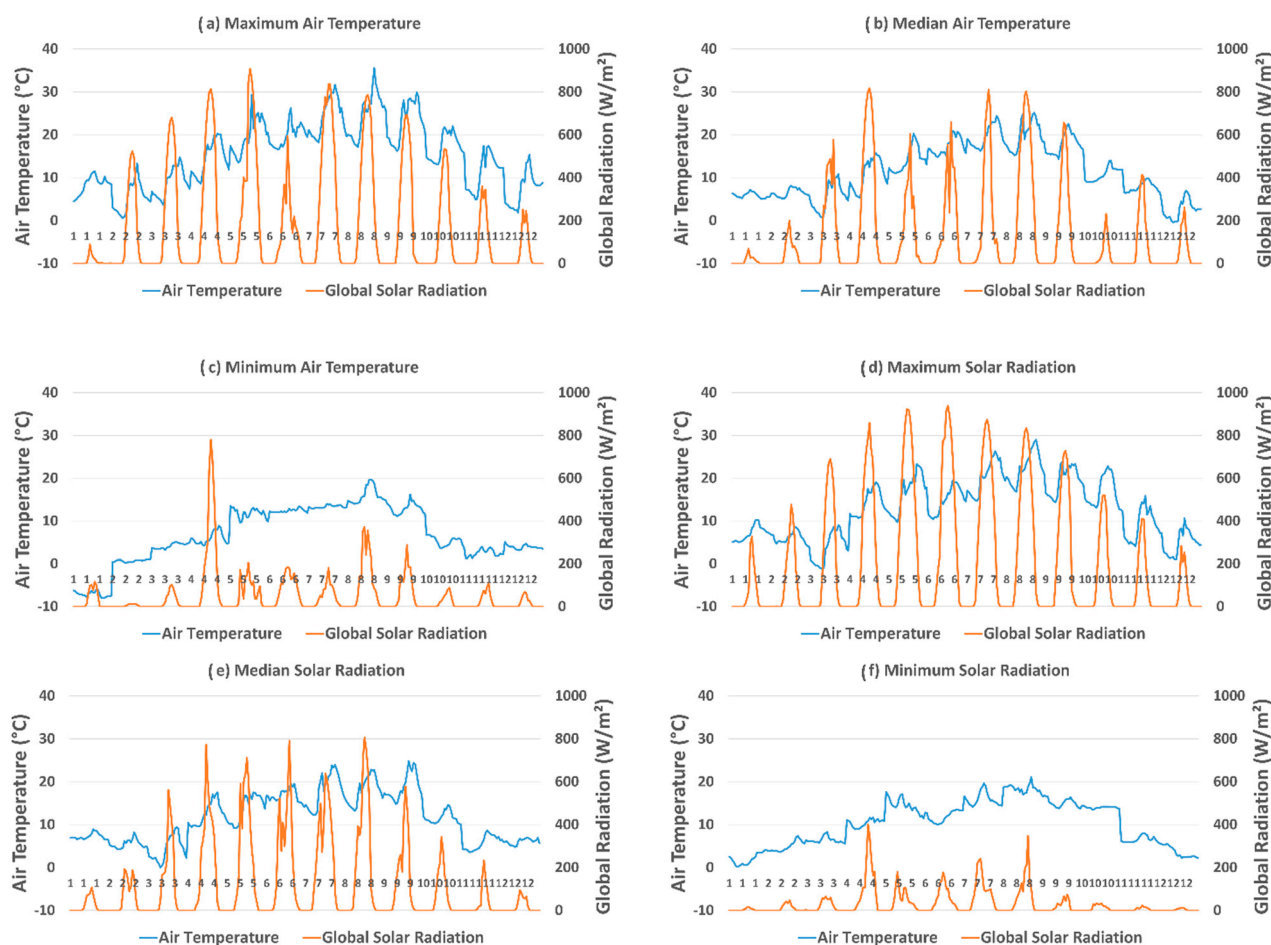


Figure 4. Hourly air temperature and solar radiation for days with maximum (a), median (b), and minimum (c) daily average temperatures and maximum (d), median (e), and minimum (f) daily total solar radiation.

3. Microclimate Modeling (ENVI-met)

The next step in the development of the ANN-based urban climate model was to generate the urban canopy temperature and windspeed (output dataset) for the weather conditions presented in the previous section (input dataset). To achieve this objective, a 3D microclimate model called ENVI-met was used. The software can simulate the microclimate conditions in an urban environment, including air temperature, relative humidity, wind speed, and radiation. ENVI-met includes features such as a 3D vegetation model capable of describing trees with different shapes and shading patterns and a feature that considers the thermal inertia of building materials. These features allow for a detailed reconstruction of an urban environment. Prior to using the tool, it was validated with measured data.

3.1. Simulation Setup

To create the computation domain, an aerial image of the study area (214 m by 172 m) was exported from Google maps, and then imported into ENVI-met's Space Module. Based on the imported image of the area and the position and dimension of the buildings, the urban geometry and the computational domain were created (see Figure 5). To reduce computational time and resources, some simplifications were made to building geometries, such as omitting windows, balconies, and architectural details, which are considered to have a small effect in the relatively large-scale urban climate modeling. The physical properties of each building and surface were defined by thermal conductivity and heat capacity, as well as the surface radiation properties, emissivity, and absorptivity. All the buildings in the area are concrete buildings with assumed construction layers of 1 cm

plaster on the exterior, followed by 12 cm insulation, and 18 cm concrete wall in the interior to satisfy the minimum R value of the building code, and the pavement between the buildings is asphalt. Using an albedo meter, the solar absorptivity of the buildings' surfaces and the pavements was determined and assigned to each surface in the ENVI-met model. The indoor temperature of the buildings was assumed to be 23 °C (average of the National Energy Code of Canada heating and cooling setpoints, 22 °C and 24 °C, respectively). The temperature, humidity, and wind speed at each grid cell were computed from the conservation of mass, momentum, and energy equations, considering the grid cells' thermal properties and exposure to convective, short-, and longwave radiation fluxes, as well as latent heat fluxes. Detailed discussion on the governing equations implemented in the model can be found in the ENVI-met user manual [39,40]. While the inlet boundary conditions are defined by the hourly varying air temperature, relative humidity, and wind speed, an outflow and zero pressure were specified at the outlet boundaries. Short- and longwave radiation were directly applied on the cells' surfaces based on their sky view factor.

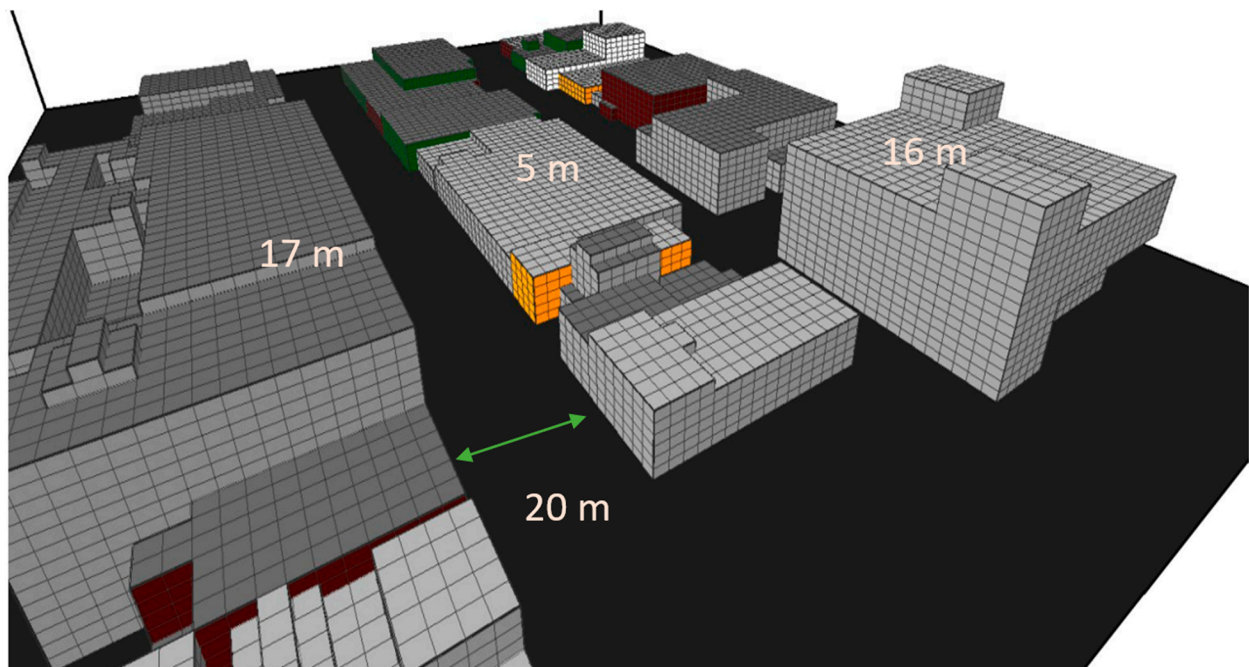


Figure 5. Created model in ENVI-met for the Study Area.

3.2. Sensitivity Study

After creating the computational domain, the various ENVI-met model settings were determined based on the sensitivity analysis results of the parameters in question, which included time step, mesh sizes, and a turbulence model. ENVI-met requires the user to specify the solver time step based on solar angle. To investigate the effect of the simulation time step on simulation results, three simulations with 2-2-1 (2 s for t_0 and t_1 , 1 for t_2), 4-4-2, and 6-6-3 values for time steps were conducted. It was determined that increasing the time step from the first setting to next had a negligible effect on air temperature values, but it reduced the simulation time by around 12% (5 h). However, increasing the time step to 4-4-2 and 6-6-3 made the simulation unstable, and resulted in the model failing. As such, a 2-2-1 solver time step and flow field, shadow and surface data update every 900 s, 600 s, and 300 s, respectively, was used.

A grid sensitivity analysis was conducted to determine the optimal space discretization beyond which further mesh refinement will not change the simulation results and will have minimal extra computation time. As such, this sensitivity study examined the grid-size impact on the simulation time and the sensitivity of the simulation results to

grid-size changes. The computational domain was discretized with three different grid sizes: $1\text{ m} \times 1\text{ m}$ (with the grid size of 1,196,208 elements), $1.5\text{ m} \times 1.5\text{ m}$ (with the grid size of 531,648 elements), and $2\text{ m} \times 2\text{ m}$ (with the grid size of 300,456 elements). The corresponding simulation results were compared. In these simulations, the grid size in the Z dimension was kept the same (1.2 m). The simulation results suggest that the air temperatures from the three meshes were comparable (the difference in air temperature was within $\pm 0.1\text{ }^\circ\text{C}$); however, the simulation time was noticeably reduced when the mesh size increased. The computational time for a 24-h simulation period (using one Core processor) was reduced from 16 days to 9 days and then to 5 days as the mesh size increased from $1\text{ m} \times 1\text{ m}$, to $1.5\text{ m} \times 1.5\text{ m}$, and to $2\text{ m} \times 2\text{ m}$, respectively. Based on the simulation results and simulation time, a $2\text{ m} \times 2\text{ m}$ grid size was adapted for this work, which consequently resulted in 230,050 elements for the $214\text{ m} \times 172\text{ m} \times 49\text{ m}$ computational domain.

Four additional simulations were carried out to assess the impact of turbulence model choice on the simulation results, comparing the four turbulence models available in ENVI-met. The results of the simulations show that the differences in air temperature were less than $0.1\text{ }^\circ\text{C}$ when using different turbulence models. The newest model, Standard TKE, which is the default for the software, showed the best stability compared to all models and the Mellor and Yamada 1982 was the least stable. As a result, the latest model was used in this study.

3.3. Validation

Prior to using the ENVI-met model, its accuracy was assessed by comparing the simulation results with onsite measured data. In the field, the temperature and relative humidity measurements were collected at 0.6 m, 1.8 m, and 3 m high from the ground (see Figure 6) using HOBO U10-003 data loggers. The data loggers have $\pm 0.5\text{ }^\circ\text{C}$ and $\pm 3.5\%$ accuracy of temperature and relative humidity, respectively. They were positioned in opaque cylindrical tubes that were wrapped with reflective tape for radiation shielding, open on both sides for ventilation, and attached at the end of square wooden sticks. A point close to building façade with an electric post was selected to attach these HOBOS.

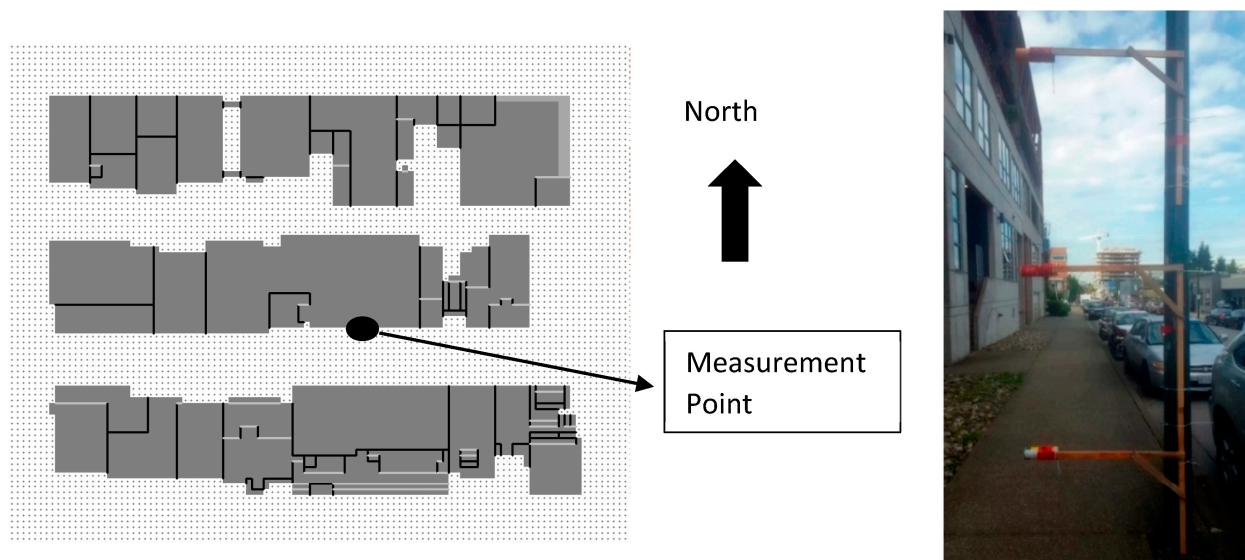


Figure 6. Measurement point and devices mounted on an electric pole at three heights (0.6 m, 1.8 m, and 3 m).

Site measurements were taken on 9 September 2021, starting from 7 a.m. to 5 p.m. After 5 p.m., the setup was removed and the measured data from the HOBOS were extracted. For the ENVI-met simulation, the hourly weather data for the same day measured at the nearby weather station were used to establish the boundary conditions. Figure 7 shows

the air temperature and airflow patterns obtained from the ENVI-met simulation at the time the field measurement was conducted. The asterisk (*) marks the temperature probe point, and the building blocks are denoted as 1, 2, and 3. In general, as the air flows from left to right, its temperature increases, as shown in the air temperature contour plots at 10 a.m. and 4 p.m. in Figure 7a. The air heating effect can be attributed to the heat transfer from the building façades and the ground, which are being heated by the solar radiation. The temperature contour plots also show relatively higher air temperatures at the section of the block where the buildings are in close proximity, 1 and 3 in contrast to 1 and 2. Moreover, the air temperature close to the south-facing façade is relatively warmer than the air temperature at the middle of the street and the air temperature close to the north-facing façade. Figure 7b shows the air temperature distribution across the street (horizontally) at 1.8 m high from the ground, and vertically 1 m away from the south-facing façade of Building 1. As can be shown in the figure on the left, the air temperature near the south-facing façade of Building 1 is consistently higher from 8 a.m. to 5 p.m. when compared to that of the north-facing façade of Building 2. The temperature difference is associated with differences in the solar heating effect of the façades due to each façade's solar orientation and shading effects. The figure on the right presents the hourly air temperature at different heights in front of the south-facing façade of Building 1. The results show vertical temperature variations along the height during the daytime. Due to the ground heating effect, the air temperature close to the ground is higher and decreases as the distance from the ground increases. At noon time, for example, the air temperature near the ground level (0.6 m) is 1.7 °C higher than the air temperature at 12 m from the ground. Figure 7c shows the airflow patterns around the buildings and the air velocity over the buildings' façades. As can be seen in the left figure, the building blocks created a Venturi effect at the beginning of the canopy and resulted in an increase in the air velocity by 40% from 1.4 m/s to 1.9 m/s. The influence of wind on the urban canopy temperature depends on the magnitude and direction of the wind. The influence of wind flowing perpendicular to the building blocks is marginal, as the air velocity within the canopy remains nearly zero. The figure on the right shows the velocity contour plots on the buildings' façades. The air velocities vary from 0 m/s (stagnation region) to 1.9 m/s around the edges of the windward surface. Establishing wind velocity distribution on building surfaces allows for proper accounting of the heat exchanges between the surrounding air and the building surfaces [41,42].

The data collected from the field measurement were used to assess the accuracy of the ENVI-met simulation. For comparison, the measured and simulated air temperature and relative humidity at the three locations was superimposed and are presented in Figure 8 and Figure 9, respectively. In general, the temperatures at all the three levels were lower in the morning for the simulation when compared to the measured values. The under prediction can be associated with not accounting for anthropogenic heat releases associated with vehicles and air conditioning units, and the over prediction in late afternoon can be related to differences in the thermal mass and surface radiation properties of the modeled and actual components. Measurement and installation errors of the HOBOs could also contribute to the differences. As expected, a reverse trend is observed for relative humidity.

The performance of the model was assessed using two error-measuring indices: Root-Mean Square Error (RMSE) and Mean Absolute Error (MAE), which were calculated using Equations (1) and (2), respectively. Table 3 provides the MAE and RMSE of the ENVI-met model for the validation case:

$$\text{RMSE} = \left[\frac{1}{n} \sum_{i=1}^n (S_i - M_i)^2 \right]^{1/2} \quad (1)$$

$$\text{MAE} = \left[\frac{1}{n} \sum_{i=1}^n |S_i - M_i| \right] \quad (2)$$

where n is the number of points; S_i is the model predicted value; and M_i is the measured value corresponding to the i th point.

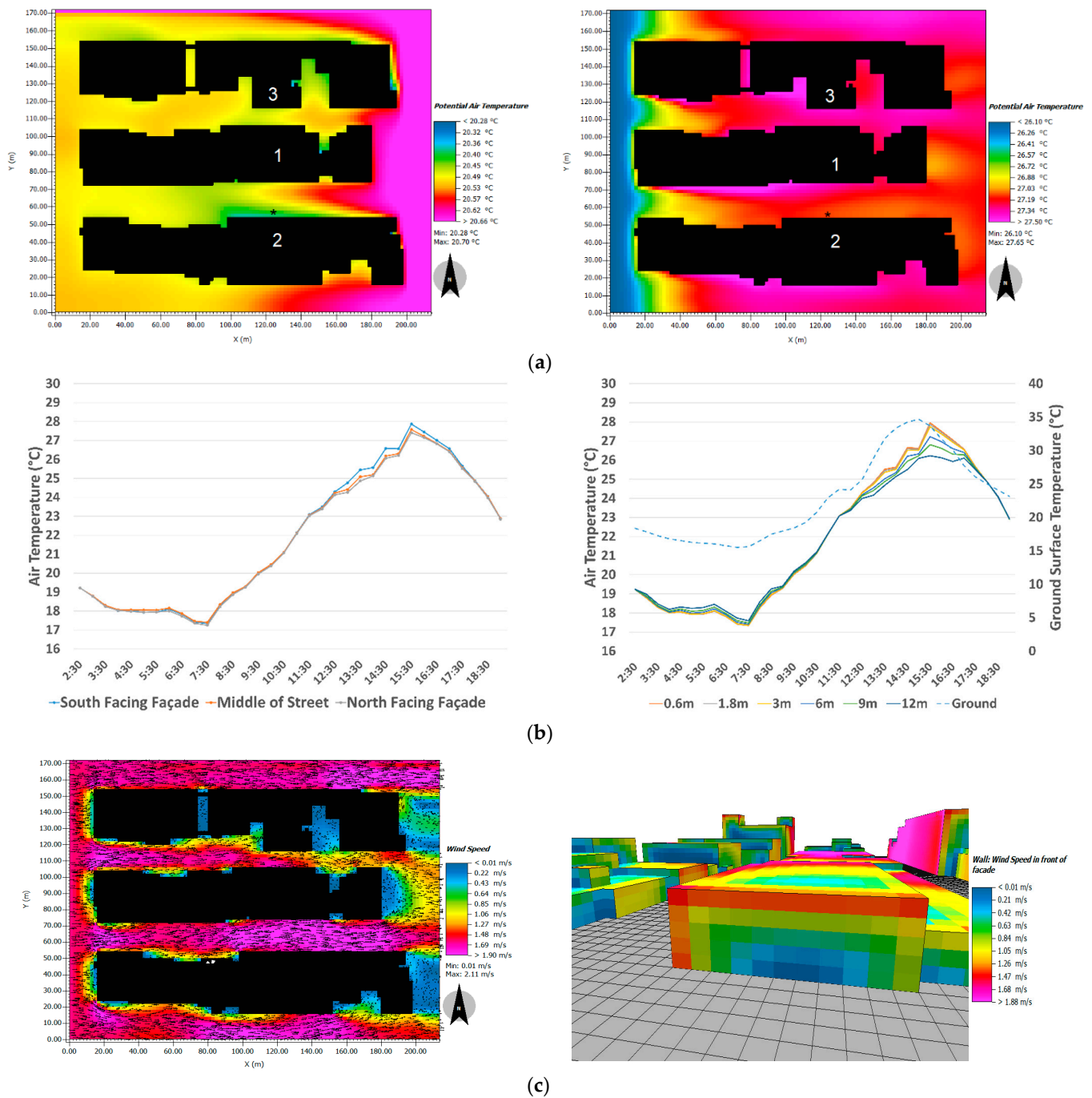


Figure 7. Air temperature and airflow profiles during the field measurement obtained from ENVI-met simulation. (a) Air temperature profiles at 1.8 m above ground at 10 a.m. (left) and 4 p.m. (right); (b) Hourly air temperature across the street at 1.8 m high from the ground (left); vertical air temperature distribution near the south-facing façade (right); (c) Airflow pattern around the buildings (left); Airflow speed along the buildings' façades (right).

As presented in Table 3, the highest RMSE and MAE values were calculated at near ground level (0.6 m from the ground), while the lowest errors were calculated at the upper position (3 m from the ground). The overall RMSE and MAE values of the simulation were

1.35 °C and 1.1 °C for temperature, respectively, and 5.12% and 4.17% for relative humidity, respectively.

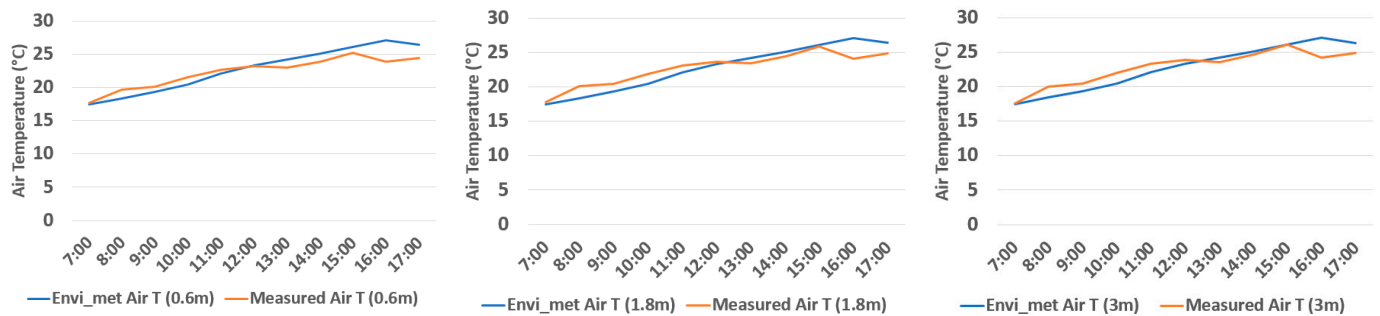


Figure 8. ENVI-met simulation results and field measurements at different heights for air T (°C).

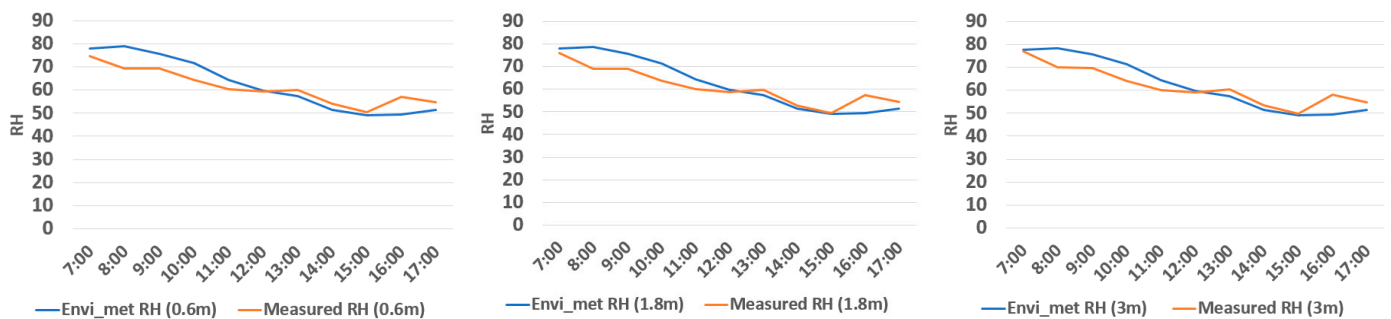


Figure 9. ENVI-met simulation results and field measurements at different heights for RH%.

Table 3. MAE and RMSE of the ENVI-met model.

Air T		
Height	Mean Absolute Error	Root Mean Square Error
Overall:	MAE: 1.1 °C	RMSE:1.35 °C
0.6 m:	MAE: 1.15 °C	RMSE:1.41 °C
1.8 m:	MAE: 1.1 °C	RMSE:1.34 °C
3 m	MAE: 1.05 °C	RMSE:1.31 °C
RH		
Overall:	MAE: 4.17%	RMSE: 5.12%
0.6 m:	MAE: 4.39%	RMSE: 5.2%
1.8 m:	MAE: 4.14%	RMSE: 5.18%
3 m	MAE: 4%	RMSE: 4.96%

Tsoka et al. (2018) [43] conducted a comprehensive literature review on the ENVI-met model’s performance by reviewing more than 50 papers. They found that for simulated air temperature, the RMSE varied from 0.5 °C to 4.3 °C with a median value of 1.51 °C and the MAE varied from 0.3 °C to 3.67 °C with a median value of 1.34 °C. Regarding relative humidity predictions, they reported that the RMSE ranged from 2% to 10% and the MAE ranged from 2.5% to 7.78%. The RMSE and MAE values obtained in this ANN model study fall within the ranges reported in [43]. Accordingly, it can be concluded that the accuracy of the ENVI-met model created in this work is acceptable and can be used to simulate the temperature and relative humidity conditions around the study area.

4. ANN Models and Urban Canopy Temperature Generation

4.1. ANN Models for Urban Air Temperature and Wind Speed Prediction

The ANN models were developed from known input and output datasets. The outputs were air temperature and wind speed extracted from the ENVI-met simulation results for those 72 representative days (1728 hourly datasets). The inputs were the corresponding meteorological data from the Vancouver International Airport (YVR) weather station. This Input–Output dataset was used for training, testing and developing the ANN models. The inputs include direct and diffuse shortwave and longwave radiation, air temperature and RH, wind speed and wind direction, and precipitation from the YVR weather station. For model warm-up and initialization, the ENVI-met simulations were conducted for 48 h instead of 24 h, and as a result the meteorological data of the previous days of 72 selected days were extracted as well. The first 24 h simulation hours were designated as warm-up periods. Results during the warm-up periods were not used for analysis, but rather to help establish better initial conditions for the day of interest (later 24 h). In general, longer warm-up periods help to reduce the impact of initial conditions on the simulation results of interest. Simulations were performed on a Dell Precision 7920 Tower PC with 192 GB RAM and 26 Core Intel Xeon Gold 6254 CPU with 3.1 GHz CPU power and each simulation (the 48-h simulation) took around 4 to 6 days. On the research PC, it was possible to run 26 simulations at the same time, as a result all 72 simulations were completed in 3 batches.

The Input–Output dataset needed to be normalized to allow all parameters to interact with one another proportionately. Normalization typically requires data to be scaled down to a range of values between 0 and 1. Here, the more conventional normalization approach, Equation (3), is used:

$$X = \frac{x - \text{mean}}{\text{Std}} \quad (3)$$

where x is the original value in dataset; mean is the mean of the original dataset; Std is the standard deviation of the original dataset; and X is the normalized value.

The normalized dataset would have a mean of 0 and a standard deviation of unity. Given that the ANN was generated using normalized data, its outputs would also be in the form of normalized data, and to transform them to the original data scale they needed to be denormalized using the corresponding mean and Std values of each parameter: $x = (X \times \text{Std}) + \text{mean}$. After normalization, the dataset was partitioned into a 75%/25% ratio for training and testing following common practice. The Latin hypercube sampling (LHS) method, which allows uniform sampling of data in the full parameter range, was used for data partitioning. In this manner, 432 data points were selected to be used for testing the performance of the ANN model, and the rest of the 1296 data points were used to train the ANN model.

In this study, feed-forward neural network types with one hidden layer were created in MATLAB. For training the ANNs, the Levenberg–Marquardt (LM) backpropagation learning algorithm was used. While a log sigmoid function was used as an activation function in the hidden layer, in the output layer, a linear function was used. The neural network training was considered to be completed when either the maximum number of training epochs was reached, or the validation performance of the neural network did not improve after six sequential epochs, which is a default setting in MATLAB. A summary of the ANN's features and the corresponding MATLAB functions is provided in Table 4. The ANN architecture adapted in this paper is similar to that of other researchers working on similar problems. The Levenberg–Marquardt (LM) backpropagation learning algorithm (`trainlm`) was used for training the ANN. Mohandes et al. (2019) [44], in a comprehensive review on the application of artificial neural networks in building energy analysis, stated that around 86% of reviewed papers used one hidden layer and used RMSE to evaluate the accuracy of ANN models. They also mentioned that the most used network type and training function were feed-forward neural network and LM backpropagation, respectively. The two ANNs for predicting urban air temperature and urban wind speed (which hereafter

are called ANN-AirTemperature and ANN-WindSpeed, developed following the stated procedure and ANN architecture) are discussed in the next section.

Table 4. ANN architecture.

	Applied ANN Features
Network Type:	Feed-forward backpropagation
Training Function:	Levenberg–Marquardt (Trainlm)
Performance Function:	RMSE
Number of Hidden Layers:	1
Activation Function:	logsig (hidden layer) and Purelin (output)

In order to determine the number of neurons in the hidden layer, six ANNs with 1, 8, 15, 17, 20, and 100 hidden neurons were evaluated. The neural network training process is inherently randomized. This means that even when they are provided with exactly the same training data, the resulting neural network model will not be identical. Accordingly, in this study, the neural networks were trained five times with the same training data and their accuracy was assessed based on their RMSE values. Table 5 provides the RMSE values of the six ANNs for the five runs. As can be seen in the table, the ANNs with hidden neuron numbers from 8 to 17 had a very similar performance and by increasing the number of hidden layers the performance of the ANN will be reduced. This is in accordance with the findings of Dong et al. (2018) [45], who proposed that the maximum number of hidden-layer neurons is to be specified as $(2 \times \text{No. inputs} + 1)$. Given that the ANN with eight hidden layers yielded the lowest overall RMSE and the lowest average RMSE of all the considered ANNs, it was adapted in the ANN-AirTemperature model used in this study. The RMSE and MAE of the created ANN-AirTemperature were 1.217 °C and 1 °C, respectively. The schematic of the ANN model with eight inputs, one output and eight hidden neurons is illustrated in Figure 10. In this figure, the numbers under Input box and Output box show the number of inputs and outputs and the number under the Hidden box shows the number of neurons.

Table 5. RMSE values for different hidden-layer neuron numbers.

Runs	Number of Neurons in Hidden Layer					
	1	8	15	17	20	100
1	1.2904	1.2121	1.2171	1.2219	1.2350	1.4055
2	1.2930	1.2190	1.2201	1.2284	1.2319	1.5064
3	1.2693	1.2170	1.2190	1.2181	1.2399	1.4118
4	1.2815	1.2191	1.2195	1.2201	1.2339	1.6395
5	1.2721	1.2184	1.2190	1.2174	1.2460	1.5508

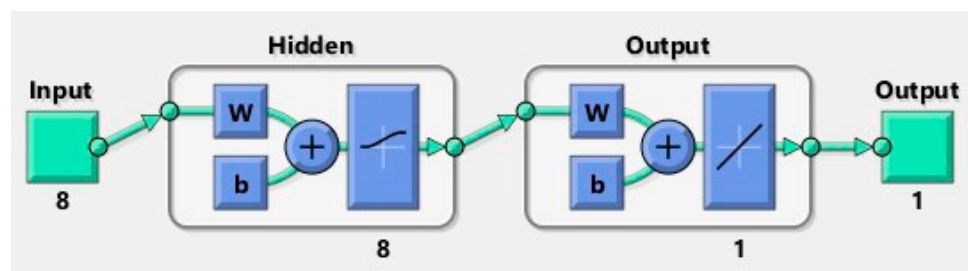


Figure 10. ANN-AirTemperature architecture.

To put the performance of the created ANN in perspective, Sahin's (2012) [46] ANN model for predicting monthly mean air temperature using remote sensing had an RMSE of 1.254 °C and Schuch et al.'s (2017) [47] ANN model had an MAE in the range of 1.3 °C to 2.3 °C. Moreover, regression models used to map the air temperature of hot summer days [13] and daily mean air temperature [12] had an RMSE of 2.31 °C and an RMSE in the range between 1.5 °C and 3.2 °C, respectively. As such, it can be said that the performance of the ANN model created for this study is acceptable and the method described can be used to generate the air temperature in the urban area using weather data from an airport weather station.

Another factor that contributes to the creation of UHI is the reduced wind speed in urban areas. Urban structures block wind speed and, as a result, the air temperature in urban areas will increase. In order to predict the urban wind speed, another artificial neural network was created to predict the hourly urban wind speed from YVR weather station data. The architecture and the procedure followed creating the ANN-WindSpeed is similar to what was described for urban air temperature. The MAE of the ANN-WindSpeed was found to be 0.44 m/s. In the Beaufort scale, a wind speed of less than 1 m/s is considered calm air. Based on this scale, it can be said that the performance of the created ANN-WindSpeed model is acceptable in predicting the wind speed in urban areas using YVR weather data.

4.2. Urban Canopy Temperature

The hourly urban canopy temperature for a whole-year period can be generated from the YVR airport weather station data using the created ANN model. First, the YVR weather parameters are normalized using the mean and standard deviation values that were established for the input parameters in Section 4.1. The process of generating the canopy air temperature is summarized in Figure 11. The urban canopy wind speed can also be generated in a similar fashion. The normalized 8760 dataset is then introduced into the ANNs as input, and the corresponding urban air temperature and wind speed are obtained as an output of the ANN models. Finally, the ANN outputs are denormalized using the mean and Stds of the outputs of the training dataset.

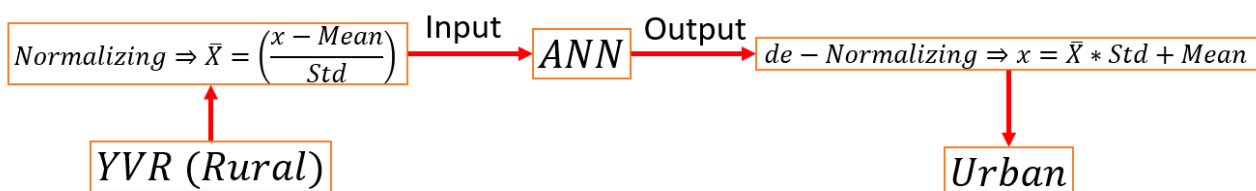


Figure 11. Process of creating urban canopy temperature and wind speed.

Figure 12 presents the hourly predicted urban canopy air temperature for the study's urban area and the air temperature recorded at the YVR weather station for the month of July as an example. The urban canopy temperature in general is 3 °C to 5 °C higher than measurements at the YVR airport during daytime and 1 °C to 2 °C higher at nighttime. Figure 13 shows the daily maximum and minimum air temperatures in the study area and the YVR weather file for the full year. As can be seen in the figure, the daily maximum and minimum temperatures are consistently higher in the urban area, and the differences in comparison to that of the airport weather station are much higher in the period from April to September. The higher temperatures in the study area are associated with the urban heat island effect. For the location, the annual average urban heat island intensity (UHII), which is defined as the average of the urban and the metrological weather station air temperature differences, is 1.7 °C. Figure 14 illustrates the maximum UHII values for each month. The highest UHII value is 7.3 °C, which is during the month of April, and the lowest monthly maximum UHII is in December. The UHII values in the winter months can be attributed mainly to the anthropogenic effect associated with heat release from vehicles and buildings and the wind-blocking effect.

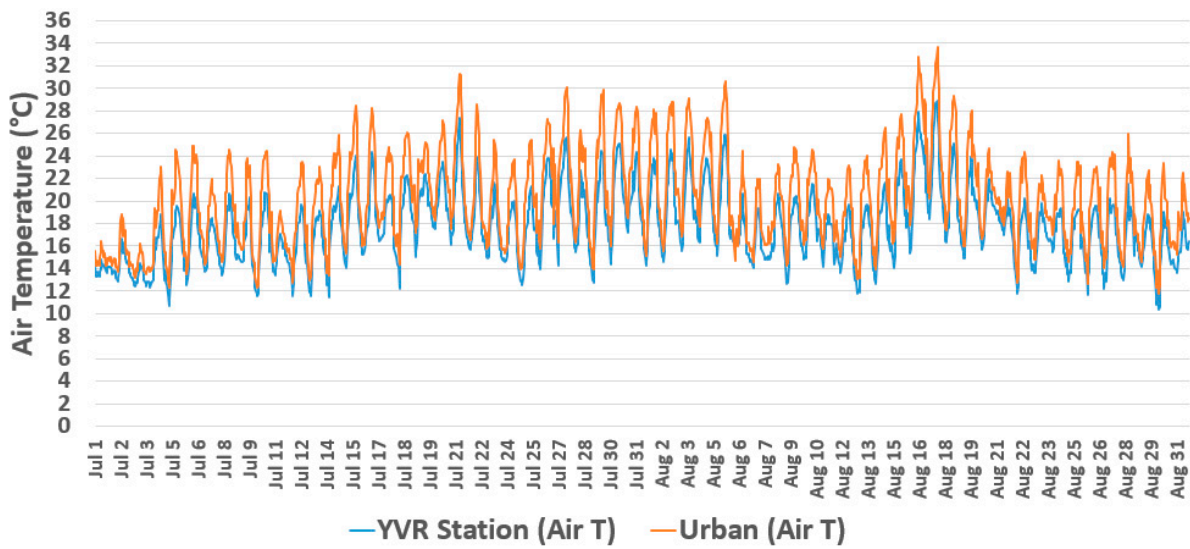


Figure 12. Urban and YVR (rural) air temperature (°C) for Vancouver city.

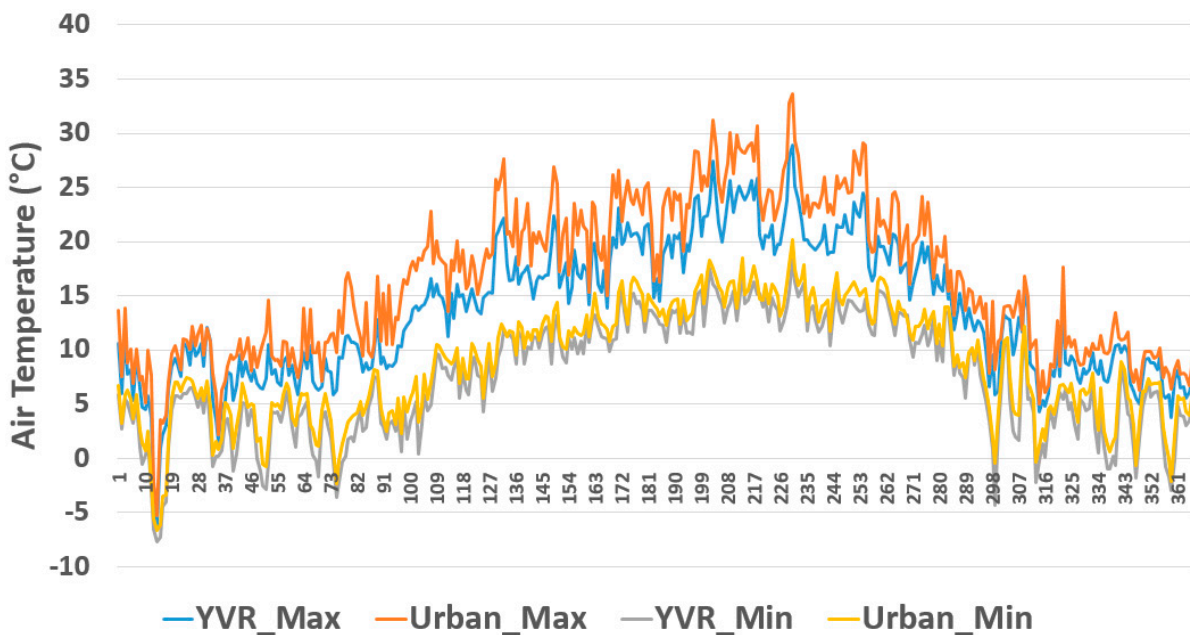


Figure 13. Daily maximum and minimum air temperature for urban and YVR weather for the full year.

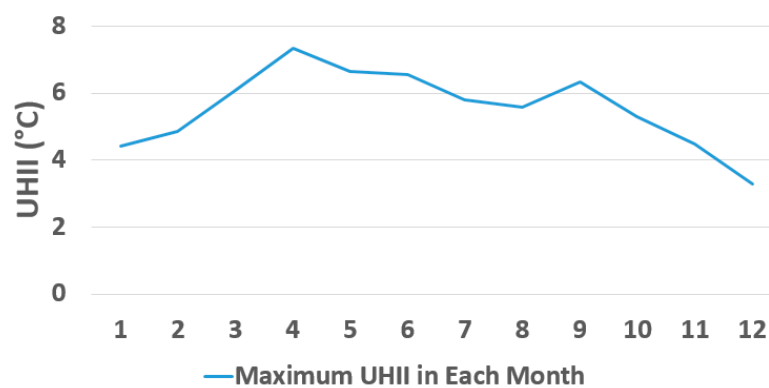


Figure 14. Maximum UHII in each month.

The monthly and hourly UHII distributions for the simulated year, categorized into two groups based on the hourly temperature differences, are presented in Figures 15 and 16, respectively. The highest percentage of occurrences with a temperature difference greater than 4 °C happen in the month of August, 22.2%, followed by 16.8% in the month of July. The high percentage of modest temperature differences (2 °C and 4 °C) are similarly found in the warmer months; August, 15% and July, 14%. Figure 16 presents the temperature difference distribution with respect to the time of day. As can be seen from the distribution, the difference in the urban and the YVR temperatures peaks at 1 p.m. About 55% of the temperature differences above 4 °C are observed between 11 a.m. and 2 p.m., and temperature differences between 2 °C and 4 °C are observed uniformly between 8 a.m. and 8 p.m.

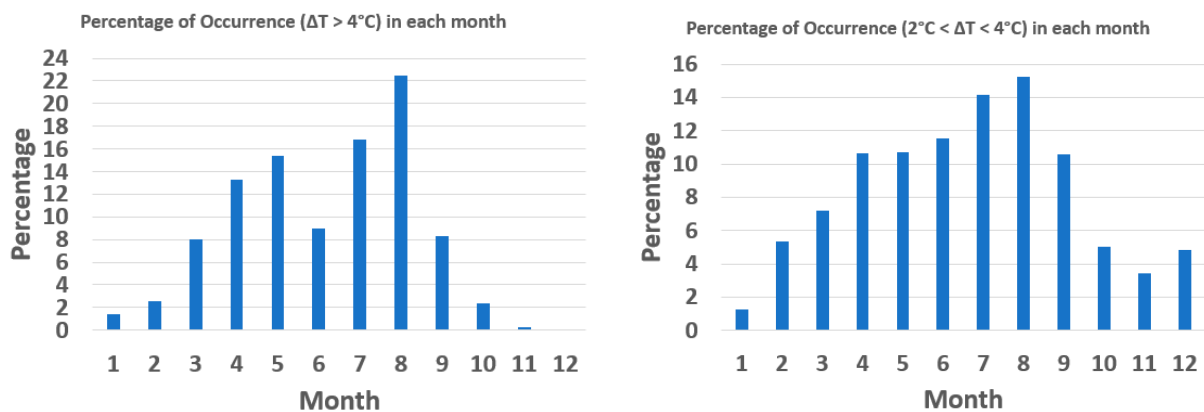


Figure 15. Monthly UHII distribution for temperature difference $>4^\circ\text{C}$ (left) and between 2°C and 4°C (right).

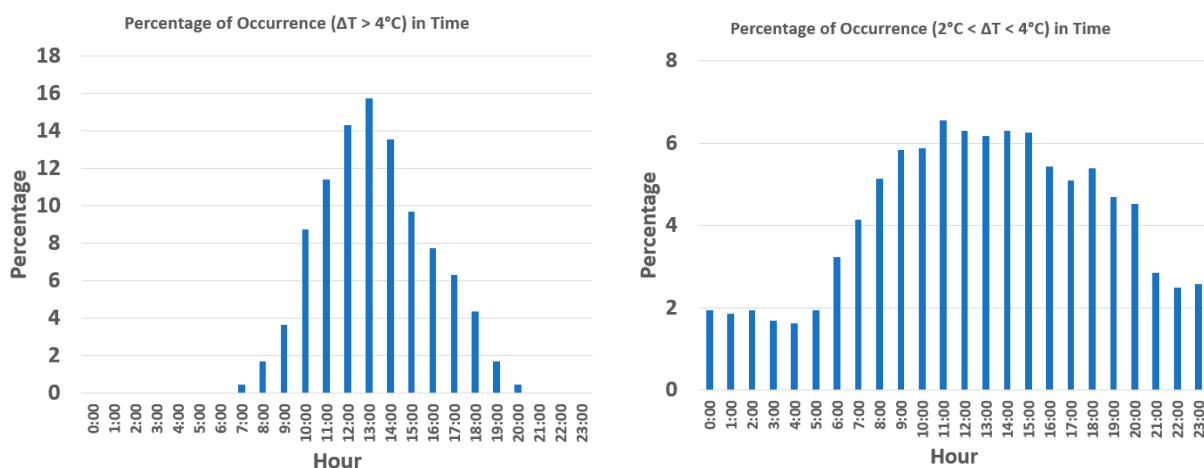


Figure 16. Hourly UHII distribution for temperature difference $>4^\circ\text{C}$ (left) and between 2°C and 4°C (right).

5. Building Energy Consumption for Heating and Cooling with UHI Effect

As has been shown in the previous section, due to the UHI effect, the air temperature in the urban area is different from the temperature measurements at the metrological weather stations in the airport or rural areas. Consequently, buildings of the same type and operation in an urban and a rural environment may have different heating and cooling energy demands. To quantify the effect of the UHI effect on the energy consumption of buildings in the Vancouver region, two office buildings with an identical design and operation were simulated in urban and rural environmental settings using the DesignBuilder energy simulation tool (software with EnergyPlus simulation engine), and their heating and cooling energy were compared. For the rural building, the YVR weather file was used, whereas

for the urban building, the air temperature and wind speed in the YVR weather file was replaced with the hourly urban canopy temperature and wind speed generated by the ANNs. As such, while the urban weather file incorporated the effect of UHI effects, the rural weather file did not.

The building type considered for the study was a two-story concrete office building with a floor area of 1216 m² (see Figure 17). As per the ASHRAE 90.1 requirements for non-residential mass buildings, the exterior walls, which are composed of 0.18 m concrete followed by 0.07 m EPS and 0.01 m plaster on the exterior, have an overall U value of 0.5 W/m²K. The metal deck roof has an overall U value of 0.18 W/m²K. The ground floor is composed of 0.15 m EPS at the bottom followed by 0.1 m concrete and 0.03 m ceramic tiles on the top, and has an overall U value of 0.25 W/m²K. The SHGC and U values of the windows are 0.38 and 1.76 W/m²K, respectively. The physical and thermal properties of the materials of different layers of the building envelope are summarized in Table 6. Following the Canadian National Building Energy Code (NECB), the building airtightness is set to 0.2 L/s/m². The buildings' internal loads including occupancy, lighting, equipment, and ventilation, and their respective operating schedules are adapted from the NECB. The cooling and heating set points are set at 24 °C and 22 °C, respectively, during the weekdays between 6 a.m. and 8 p.m. During all other times, the cooling system is off and a setback temperature of 18 °C is enforced during the heating season.

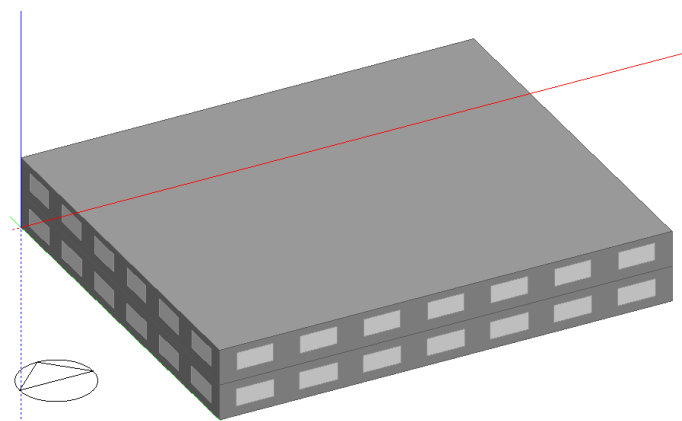


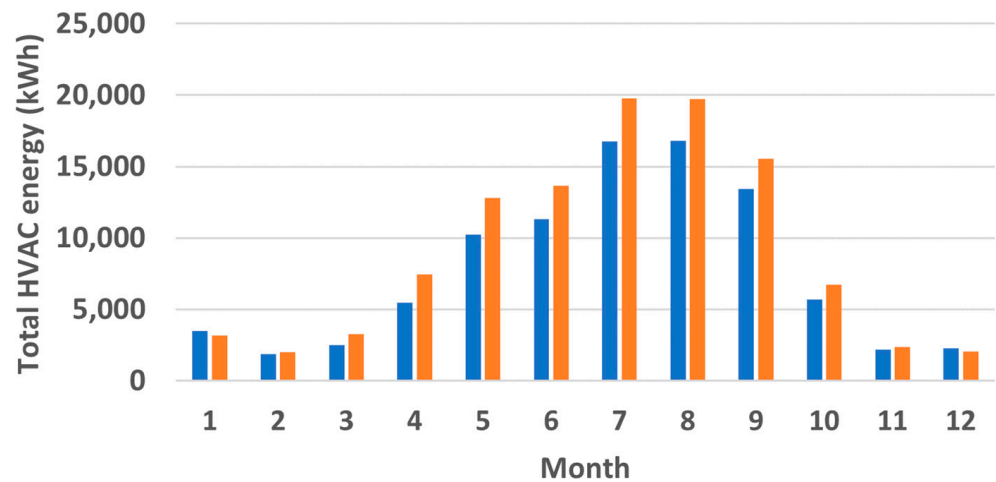
Figure 17. Modeled building in DesignBuilder.

Table 6. Physical and thermal properties of the building envelope materials.

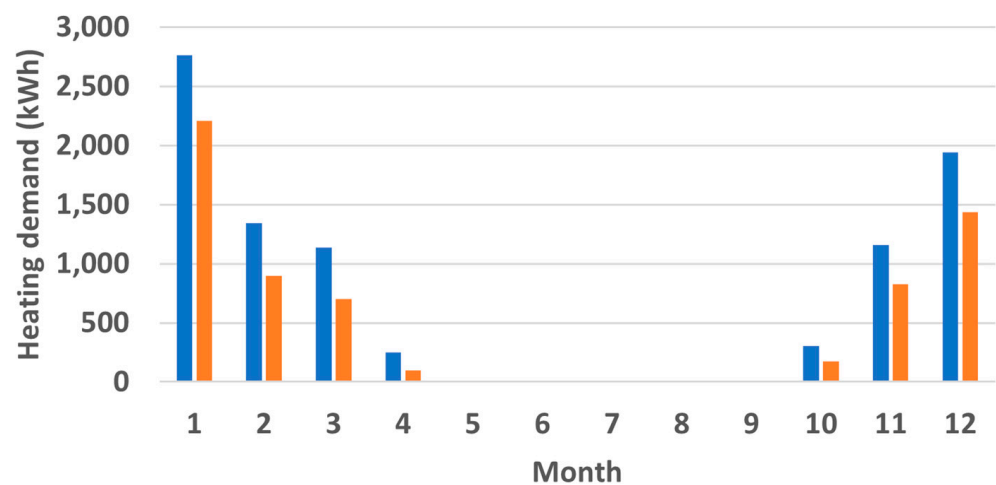
Material	Property			
	Thickness (m)	Density (Kg/m ³)	Conductivity (W/mK)	Specific Heat (J/KgK)
XPS	0.18	35	0.034	1400
Concrete	0.18 and 0.1	2220	1.6	850
EPS	0.07 and 0.147	15	0.04	1400
Plaster	0.01	1500	0.6	850
Ceramic Tile	0.03	1700	0.8	850

Figure 18 shows the monthly heating, cooling, and total energy consumption of the buildings in the study area (urban environment) and the YVR airport (rural environment). As the buildings are office buildings with significant internal gains, the cooling energy demand in the summer months is much higher than the heating energy demand in the heating season (roughly one-to-ten ratio), as illustrated in Figure 18a. During the colder months, the heating energy consumption of the building in the study area was consistently lower than that of the building at YVR (Figure 18b). The reduction in energy consumption

during the months of December, January, and February was 26%, 20%, and 33%, respectively. The decrease in heating energy in the study area is associated with the higher canopy air temperature as the result of the urban heat island effect, as well as the reduction in air flow speed due to the wind-blockage effect of buildings. Due to the same effects, the buildings' energy consumption in the warmer months was in inverse order (Figure 18c). The highest cooling demands were in July and August, and during these months the buildings in the urban environment had a cooling energy demand of 17% and 18% more, respectively, than that of the building at YVR airport. In Table 7, the annual heating, cooling, and total energy demands of the buildings are presented. As was expected, the urban heat island effect increased the total cooling energy demand by 23% and decreased the total heating energy consumption by 29%. Although the percentage change for heating is higher, the magnitude of the cooling energy difference is much higher. As such, the total energy demand of the building in the urban area is 18% higher, which points to the overall negative effect of the urban island effect in that significant increases in cooling counteract the benefit obtained in the reduction in heating in the winter season.



(a) ■ Baseline (YVR) ■ Urban Weather File



(b) ■ Baseline (YVR) ■ Urban Weather File

Figure 18. Cont.

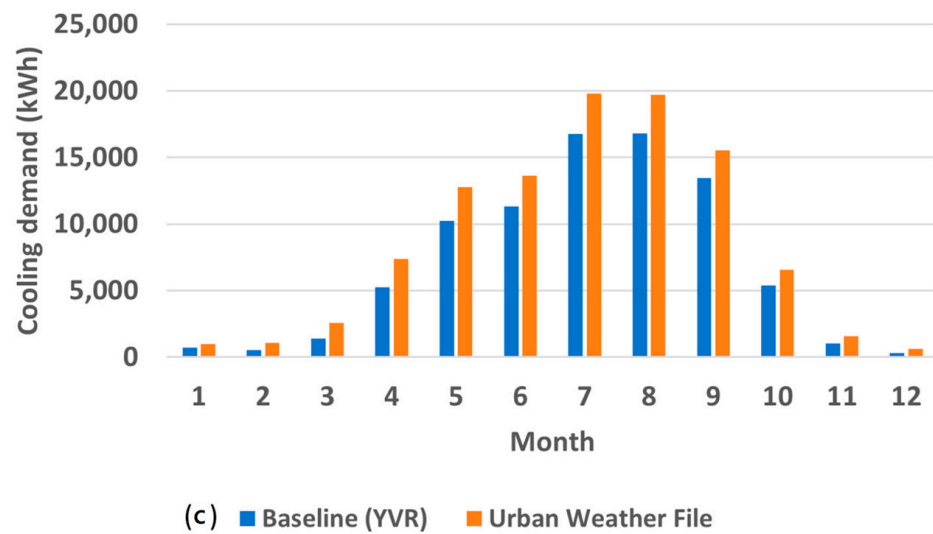


Figure 18. Cooling, heating, and total energy consumption (kWh) using urban and YVR weather file. (a) shows the total HVAC energy consumption in each month; (b) shows the energy consumption required for heating in each month; (c) shows the energy required for cooling in each month.

Table 7. Building energy consumption comparison for Vancouver city.

	Percentage of Change (UHI Affected—Baseline (YVR))
Total Heating:	−29% (−1.08 kWh/m ²)
Total Cooling:	23% (8.09 kWh/m ²)
Total Energy:	18% (7.01 kWh/m ²)

Figure 19 illustrates the distribution of the indoor air temperature presented as the number of hours at or above the specified temperature values. The number of hours of indoor temperature above the cooling set point, 25 °C and above, for the building at YVR is 2165 h, while in the presence of the urban heat island, the number of hours would increase to 2330 h, which is an increase of 7.6%. These results suggest that the UHI effect increases the overheating potential of buildings in the urban setting, and the use of airport weather data underestimates the thermal discomfort that may exist in the urban buildings.

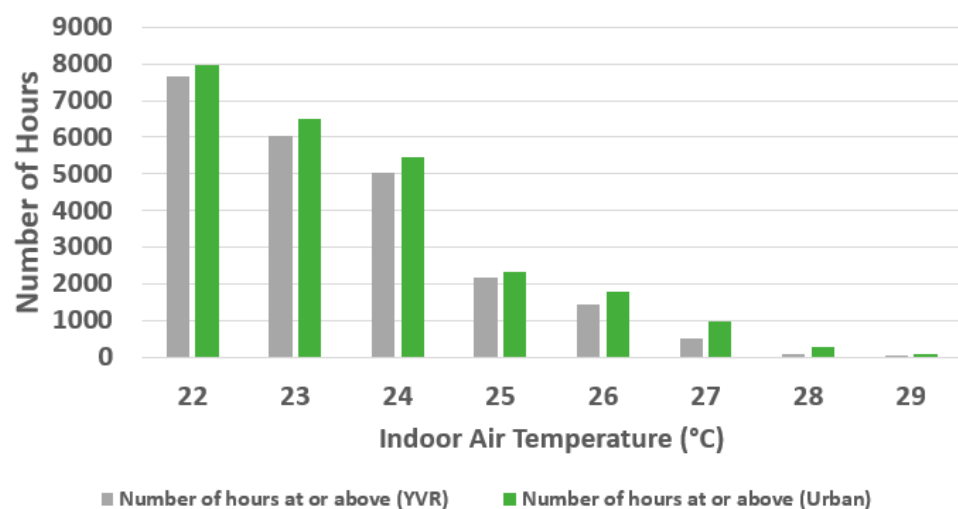


Figure 19. Indoor air temperature distribution (°C) for urban and YVR weather files.

6. Conclusions

The urban heat island phenomenon is a reality in cities worldwide and has been reported in several studies. It is essential to know the level to which the urban canopy temperature rise due to the UHI effect and its consequences on urban thermal discomfort and buildings' energy consumption. Ignoring the UHI effect on the local temperature and the use of weather data from open fields and airport locations leads to over- and under-estimation of heating and cooling loads and improper sizing of equipment. Improper sizing leads the mechanical systems to operate outside their ideal range on their performance curves resulting in higher energy consumption (inefficiency) and occupants' thermal discomfort.

In this paper, a method to estimate urban canopy temperature was presented. In this method, the urban temperature was predicted from weather data collected at an airport or open field using an artificial neural network model. The method enables the generation of hourly urban weather data for a whole-year building energy simulation. In this work, it was used to predict the urban canopy temperature of a neighborhood in downtown Vancouver and the resulting building energy consumption and indoor temperature. The predicted daily maximum and minimum temperatures in the neighborhood were consistently higher than at the airport weather station. For the location and the time period considered in this study, the annual average urban heat island intensity (UHII), which is defined as the average of the urban and the metrological weather station air temperature differences, was 1.7 °C. The highest percentage of UHII occurrences with a temperature difference greater than 4 °C happened in the month of August, 22.2%, followed by 16.8% in the month of July. The urban heat island effect increased the total cooling energy demand by 23% and decreased the total heating energy consumption by 29%. Although the percentage change for heating is higher, the magnitude of the cooling energy difference is much higher. As such, the total energy demand of the building in the urban area is 18% higher, which points to the overall negative effect of the urban heat island effect in that significant increases in cooling counteract the benefit obtained in the reduction in heating in the winter season. The urban heat island effect in the study area increases the number of hours of indoor temperature above the cooling set point by 7.6% when compared to a building in a rural environment. These results suggest that the UHI effect increases the overheating potential of buildings in the urban setting, and the use of airport weather data underestimates the thermal discomfort that may exist in the urban buildings. The methodology provided in this paper can be applied to determine the varying, urban heat island effects in different climate zones.

Author Contributions: Conceptualization, F.T.; Methodology, F.T. and A.G.M.; Software, A.G.M.; Formal analysis, A.G.M.; Investigation, F.T.; Writing—original draft, F.T. and A.G.M.; Visualization, A.G.M.; Project administration, F.T.; Funding acquisition, F.T. All authors have read and agreed to the published version of the manuscript.

Funding: The authors are grateful for the financial support provided by the Natural Sciences and Engineering Research Council of Canada (NSERC) IC-IMPACTS.

Acknowledgments: The authors are grateful for the support provided by the IC-IMPACTS, Natural Sciences and Engineering Research Council of Canada (NSERC), Canada Research Chair (CRC), and the School of Construction and the Environment at the British Columbia Institute of Technology (BCIT).

Conflicts of Interest: The authors declare no conflict of interest.

References

1. Gui, J.; Phelan, P.E.; Kaloush, K.E.; Golden, J.S. Impact of pavement thermophysical properties on surface temperatures. *J. Mater. Civ. Eng.* **2007**, *19*, 683–690. [[CrossRef](#)]
2. Yamagata, H.; Nasu, M.; Yoshizawa, M.; Miyamoto, A.; Minamiyama, M. Heat island mitigation using water retentive pavement sprinkled with reclaimed wastewater. *Water Sci. Technol.* **2008**, *57*, 763–771. [[CrossRef](#)] [[PubMed](#)]

3. Chen, F.; Kusaka, H.; Bornstein, R.; Ching, J.; Grimmond, C.S.B.; Grossman-Clarke, S.; Loridan, T.; Manning, K.W.; Martilli, A.; Miao, S.; et al. The integrated WRF/urban modelling system: Development, evaluation, and applications to urban environmental problems. *Int. J. Climatol.* **2011**, *31*, 273–288. [[CrossRef](#)]
4. Li, Y.; Zhao, X. An empirical study of the impact of human activity on long-term temperature change in China: A perspective from energy consumption. *J. Geophys. Res. Atmos.* **2012**, *117*, 17117. [[CrossRef](#)]
5. Li, H. *Pavement Materials for Heat Island Mitigation: Design and Management Strategies*; Butterworth-Heinemann: Oxford, UK, 2015.
6. Akbari, H. *Energy Saving Potentials and Air Quality Benefits of Urban Heat Island Mitigation*; Ernest Orlando Lawrence Berkeley National Laboratory: Berkeley, CA, USA, 2005.
7. Li, X.; Zhou, Y.; Yu, S.; Jia, G.; Li, H.; Li, W. Urban heat island impacts on building energy consumption: A review of approaches and findings. *Energy* **2019**, *174*, 407–419. [[CrossRef](#)]
8. Magli, S.; Lodi, C.; Lombroso, L.; Muscio, A.; Teggi, S. Analysis of the urban heat island effects on building energy consumption. *Int. J. Energy Environ. Eng.* **2015**, *6*, 91–99. [[CrossRef](#)]
9. Ma, Y.X.; Yu, C. Impact of meteorological factors on high-rise office building energy consumption in Hong Kong: From a spatiotemporal perspective. *Energy Build.* **2020**, *228*, 110468. [[CrossRef](#)]
10. Guattari, C.; Evangelisti, L.; Balaras, C.A. On the assessment of urban heat island phenomenon and its effects on building energy performance: A case study of Rome (Italy). *Energy Build.* **2018**, *158*, 605–615. [[CrossRef](#)]
11. Liu, Y.; Stouffs, R.; Tablada, A.; Wong, N.H.; Zhang, J. Comparing micro-scale weather data to building energy consumption in Singapore. *Energy Build.* **2017**, *152*, 776–791. [[CrossRef](#)]
12. Emamifar, S.; Rahimikhoob, A.; Noroozi, A. Daily mean air temperature estimation from MODIS land surface temperature products based on M5 model tree. *Int. J. Climatol.* **2013**, *33*, 3174–3181. [[CrossRef](#)]
13. Ho, H.C.; Knudby, A.; Sirovyak, P.; Xu, Y.; Hodul, M.; Henderson, S.B. Mapping maximum urban air temperature on hot summer days. *Remote Sens. Environ.* **2014**, *154*, 38–45. [[CrossRef](#)]
14. Masson, V. A Physically-Based Scheme For The Urban Energy Budget In Atmospheric Models. *Bound.-Layer Meteorol.* **2000**, *94*, 357–397. [[CrossRef](#)]
15. Aoyagi, T.; Seino, N. A Square Prism Urban Canopy Scheme for the NHM and Its Evaluation on Summer Conditions in the Tokyo Metropolitan Area, Japan. *J. Appl. Meteorol. Climatol.* **2011**, *50*, 1476–1496. [[CrossRef](#)]
16. Kusaka, H.; Kondo, H.; Kikegawa, Y.; Kimura, F. A Simple Single-Layer Urban Canopy Model For Atmospheric Models: Comparison With Multi-Layer And Slab Models. *Bound. Layer Meteorol.* **2001**, *101*, 329–358. [[CrossRef](#)]
17. Marciotto, E.R.; Oliveira, A.P.; Hanna, S.R. Modeling study of the aspect ratio influence on urban canopy energy fluxes with a modified wall-canyon energy budget scheme. *Build. Environ.* **2010**, *45*, 2497–2505. [[CrossRef](#)]
18. Afshari, A.; Ramirez, N.; Pasha, Y. Increasing the Accuracy of Radiation Heat Transfer Estimation in a Lumped Parameter Urban Canopy Models. *Energy Procedia* **2019**, *158*, 5181–5187. [[CrossRef](#)]
19. Bueno, B.; Nakano, A.; Norford, L.; Reinhart, C. Urban Weather Generator—A Novel Workflow for Integrating Urban Heat Island Effect within Urban Design Process. In Proceedings of the 14th Conference of International Building Performance Simulation Association, BS2015. Hyderabad, India, 7–9 December 2015.
20. Martin, M.; Afshari, A.; Armstrong, P.R.; Norford, L.K. Estimation of urban temperature and humidity using a lumped parameter model coupled with an EnergyPlus model. *Energy Build.* **2015**, *96*, 221–235. [[CrossRef](#)]
21. Bueno, B.; Norford, L.; Hidalgo, J.; Pigeon, G. The urban weather generator. *J. Build. Perform. Simul.* **2012**, *6*, 269–281. [[CrossRef](#)]
22. Bueno, B.; Norford, L.; Pigeon, G.; Britter, R. A resistance-capacitance network model for the analysis of the interactions between the energy performance of buildings and the urban climate. *Build. Environ.* **2012**, *54*, 116–125. [[CrossRef](#)]
23. Bueno, B.; Pigeon, G.; Norford, L.K.; Zibouche, K.; Marchadier, C. Development and evaluation of a building energy model integrated in the TEB scheme. *Geosci. Model Dev.* **2012**, *5*, 433–448. [[CrossRef](#)]
24. Allegrini, J.; Dorer, V.; Carmeliet, J. Influence of morphologies on the microclimate in urban neighbourhoods. *J. Wind Eng. Ind. Aerodyn.* **2015**, *144*, 108–117. [[CrossRef](#)]
25. Allegrini, J.; Dorer, V.; Carmeliet, J. Coupled CFD, radiation and building energy model for studying heat fluxes in an urban environment with generic building configurations. *Sustain. Cities Soc.* **2015**, *19*, 385–394. [[CrossRef](#)]
26. Aboelata, A.; Sodoudi, S. Evaluating urban vegetation scenarios to mitigate urban heat island and reduce buildings' energy in dense built-up areas in Cairo. *Build. Environ.* **2019**, *166*, 106407. [[CrossRef](#)]
27. Castaldo, V.L.; Pisello, A.L.; Piselli, C.; Fabiani, C.; Cotana, F.; Santamouris, M. How outdoor microclimate mitigation affects building thermal-energy performance: A new design-stage method for energy saving in residential near-zero energy settlements in Italy. *Renew. Energy* **2018**, *127*, 920–935. [[CrossRef](#)]
28. Fatima, S.; Chaudhry, H. Steady-state CFD modelling and experimental analysis of the local microclimate in Dubai (UAE). *Sustain. Build.* **2017**, *2*, 5. [[CrossRef](#)]
29. Toparlar, Y.; Blocken, B.; Maiheu, B.; van Heijst, G.J.F. Impact of urban microclimate on summertime building cooling demand: A parametric analysis for Antwerp 2017, Belgium. *Appl. Energy* **2018**, *228*, 852–872. [[CrossRef](#)]
30. Ma, L.; Bo-ot, L.M.; Wang, Y.-H.; Chiang, C.-M.; Lai, C. Effects of a Green Space Layout on the Outdoor Thermal Environment at the Neighborhood Level. *Energies* **2012**, *5*, 3723. [[CrossRef](#)]
31. Maragkogiannis, K.; Kolokotsa, D.; Maravelakis, E.; Konstantaras, A. Combining terrestrial laser scanning and computational fluid dynamics for the study of the urban thermal environment. *Sustain. Cities Soc.* **2014**, *13*, 207–216. [[CrossRef](#)]

32. Allegrini, J.; Carmeliet, J. Coupled CFD and building energy simulations for studying the impacts of building height topology and buoyancy on local urban microclimates. *Urban Clim.* **2017**, *21*, 278–305. [CrossRef]
33. Allegrini, J.; Carmeliet, J. Simulations of local heat islands in Zürich with coupled CFD and building energy models. *Urban Clim.* **2018**, *24*, 340–359. [CrossRef]
34. Chan, A.L.S. Developing a modified typical meteorological year weather file for Hong Kong taking into account the urban heat island effect. *Build. Environ.* **2011**, *46*, 2434–2441. [CrossRef]
35. Salvati, A.; Coch, H.; Morganti, M. Effects of urban compactness on the building energy performance in Mediterranean climate. *Energy Procedia* **2017**, *122*, 499–504. [CrossRef]
36. Salvati, A.; Coch Roura, H.; Cecere, C. Assessing the urban heat island and its energy impact on residential buildings in Mediterranean climate: Barcelona case study. *Energy Build.* **2017**, *146*, 38–54. [CrossRef]
37. Palme, M.; Inostroza, L.; Villacreses, G.; Lobato-Cordero, A.; Carrasco, C. From urban climate to energy consumption. Enhancing building performance simulation by including the urban heat island effect. *Energy Build.* **2017**, *145*, 107–120. [CrossRef]
38. Litardo, J.; Palme, M.; Borbor-Cordova, M.; Caiza, R.; Macias, J.; Hidalgo-Leon, R.; Soriano, G. Urban Heat Island intensity and buildings' energy needs in Duran, Ecuador: Simulation studies and proposal of mitigation strategies. *Sustain. Cities Soc.* **2020**, *62*, 102387. [CrossRef]
39. Bruse, M.; Fleer, H. Simulating surface–plant–air interactions inside urban environments with a three dimensional numerical model. *Environ. Model. Softw.* **1998**, *13*, 373–384. [CrossRef]
40. Simon, H.; Bruse, M.; Kissel, L. Evaluation of ENVI-Met's Multiple-Node Model and Estimation of Indoor Climate. Available online: https://www.researchgate.net/publication/318561953_Evaluation_of_ENVI-met\T1\textquoterights_multiple-node_model_and_estimation_of_indoor_climate (accessed on 14 May 2023).
41. Awol, D.A.; Bitsuamlak, G.T.; Tariku, F. Numerical estimation of the external convective heat transfer coefficient for buildings in an urban-like setting. *Build. Environ.* **2020**, *169*, 106557. [CrossRef]
42. Kahsay, M.; Bitsuamlak, G.T.; Tariku, F. Effect of localized exterior convective heat transfer on high-rise building energy consumption. *Build. Simul. J.* **2020**, *13*, 127–139. [CrossRef]
43. Tsoka, S.; Tsikaloudaki, A.; Theodosiou, T. Analyzing the ENVI-met microclimate model's performance and assessing cool materials and urban vegetation applications—A review. *Sustain. Cities Soc.* **2018**, *43*, 55–76. [CrossRef]
44. Mohandes, S.R.; Zhang, X.; Mahdiyar, A. A comprehensive review on the application of artificial neural networks in building energy analysis. *Neurocomputing* **2019**, *340*, 55–75. [CrossRef]
45. Dong, Q.; Xing, K.; Zhang, H. Artificial Neural Network for Assessment of Energy Consumption and Cost for Cross Laminated Timber Office Building in Severe Cold Regions. *Sustainability* **2018**, *10*, 84. [CrossRef]
46. Şahin, M. Modelling of air temperature using remote sensing and artificial neural network in Turkey. *Adv. Space Res.* **2012**, *50*, 973–985. [CrossRef]
47. Schuch, F.; Marpu, P.; Masri, D.; Afshari, A. Estimation of Urban Air Temperature From a Rural Station Using Remotely Sensed Thermal Infrared Data. *Energy Procedia* **2017**, *143*, 519–525. [CrossRef]

Disclaimer/Publisher's Note: The statements, opinions and data contained in all publications are solely those of the individual author(s) and contributor(s) and not of MDPI and/or the editor(s). MDPI and/or the editor(s) disclaim responsibility for any injury to people or property resulting from any ideas, methods, instructions or products referred to in the content.